

Numerical Simulation of the Structure and Mechanical Properties of Silicene Layers on Graphite during the Lithium Ion Motion

A. E. Galashev^{a,*} and K. A. Ivanichkina^a

^a *Institute of High-Temperature Electrochemistry, Ural Branch, Russian Academy of Sciences, Yekaterinburg, 620137 Russia*

*e-mail: galashev@ihte.uran.ru

Received May 28, 2018

Abstract—The molecular dynamics method is applied to study structural and mechanical effects appearing during the lithium ion motion in a dc electric field along a planar channel formed by perfect silicene sheets and sheets containing vacancy-type defects. Mono-, di-, tri-, and hexavacancies of rather densely and uniformly filled silicene sheets are arranged one above the other on a graphite substrate. The times of Li^+ ion passage through silicene channels with various gaps are determined. The construction of Voronoi polyhedra and truncated polyhedrons, whose centers coincide with the moving ion position allowed revealing the structural features inherent to the two-dimensional layered structure. The nature of stresses appearing in silicene sheets most critical to ion motion over the channel is determined.

DOI: 10.1134/S1063783419020136

1. INTRODUCTION

Usual lithium-ion batteries based on graphite anodes cannot provide any longer satisfactory productivity, which includes high capacitance, high speed, good cyclicality, and low price [1–3].

Two-dimensional (2D) materials are major candidates to be an anode material and have recently attracted considerable attention due to their unique structural properties [4–6]. The point is that the two-dimensional structure can provide a larger surface area for disposing of lithium atoms. Furthermore, loose packing between two-dimensional layers can facilitate volume extension and compression caused by intercalation and deintercalation of lithium atoms. Most silicenes synthesized to date are deposited on metal substrates such as Ag(111) and Ir(111) [7, 8]. The strong interaction between substrates and silicene grown on them perturbs the electronic structure of freestanding silicene [9, 10] and can induce surface reconstruction [11]. As a result, very important promising properties of freestanding silicene necessary for its applications as an anode material are lost. Molecular-dynamics simulation showed that graphene can be used as a substrate for silicene instead of metal substrates [12, 13]. In contrast to metal substrates, the interaction between silicene and graphene is mainly controlled by Van der Waals forces, due to which unique silicene properties can be retained. However, the application of graphene for supporting silicene can currently be considered to be no more than a hypothetical feasibility. The nanocomposite fabrication technology is not

developed. The quasi-continuous layer of two-dimensional silicon on the inert highly oriented pyrolytic graphite (HOPG) substrate was obtained at room temperature under ultrahigh vacuum conditions in [14]. The presence of a small number of HOPG regions existing together with formed small 3D Si clusters was found. Scanning tunneling microscopy data indicate the presence of a very small strain (0.05 nm) in silicene. Van der Waals forces create the silicene–surface bond. The existence of such interaction makes the perfect silicene monolayer on the HOPG surface stable at both room temperature and at 350°C. The silicene growth on the nonmetal inert substrate is an important step in the way to obtaining silicon layers containing no alloys and having properties close to freestanding silicene. Silicene offers prospects of full compatibility of its application with already existing silicon technologies. Furthermore, silicene on the graphite substrate represents a less expensive decision than technologies based on silver substrates [15]. The studies presented in [15] point to fundamental difficulties in the use of silicene sheets on silver substrates as an electrode of lithium-ion batteries.

The objective of this work is to study the applicability of layered silicon such as silicene sheets as a material of the lithium-ion battery anode. The calculations were performed using the LAMMPS package codes [16] and the “URAN” hybrid cluster-type computer of the Institute of Mathematics and Mechanics, Ural Branch of Russian Academy of Sciences.

2. NUMERICAL MODEL

The Si–Si, Si–C, and C–C interatomic interactions were presented by the Tersoff many-body potential [17, 18]

$$V_{ij} = f_C(r_{ij})[A \exp(-\lambda^{(1)} r_{ij}) - B b_{ij} \exp(-\lambda^{(2)} r_{ij})], \quad (1)$$

$$f_C(r_{ij}) = \begin{cases} 1, & r_{ij} < R^{(1)} \\ \frac{1}{2} + \frac{1}{2} \cos \left[\frac{\pi(r_{ij} - R^{(1)})}{(R^{(2)} - R^{(1)})} \right], & R^{(1)} < r_{ij} < R^{(2)} \\ 0, & r_{ij} > R^{(2)} \end{cases}, \quad (2)$$

$$b_{ij} = (1 + \beta^n \xi_{ij}^n)^{-1/(2n)},$$

$$\xi_{ij} = \sum_{k \neq i, j} f_C(r_{ij}) g(\theta_{ijk}),$$

$$g(\theta_{ijk}) = 1 + \frac{c^2}{d^2} - \frac{c^2}{[d^2 + (h - \cos \theta_{ijk})]}.$$

During the interaction of atoms belonging to components p and q , the parameters $\lambda^{(1)}$, $\lambda^{(2)}$, A , B , $R^{(1)}$, and $R^{(2)}$ are given by

$$\lambda^{(k)} = (\lambda_p^{(k)} + \lambda_q^{(k)})/2; \quad A = (A_p A_q)^{1/2};$$

$$B = (B_p B_q)^{1/2};$$

$$R^{(1)} = (R_p^{(1)} R_q^{(1)})^{1/2}; \quad R^{(2)} = (R_p^{(2)} R_q^{(2)})^{1/2}.$$

Here the parameters A and B are energy characteristics of repulsion and attraction; the many-body parameter b_{ij} depends on local atom coordination around atom i ; the parameters $\lambda^{(1)}$ and $\lambda^{(2)}$ with the dimension of the inverse length set the degree of repulsion and attraction, respectively; the parameters $R^{(1)}$ and $R^{(2)}$ with dimension of length were chosen so that only nearest neighbors are taken into consideration; the parameters n , n_i , and β define the bonding force acting on atoms depending on an ambient medium environment; ξ_{ij} is the effective coordination number; indices i , j , k denote carbon atoms; r_{ij} is the i – j bond length; θ_{ijk} is the angle between i – j and j – k bonds; $g(\theta_{ijk})$ is the function of this angle, stabilizing the structure; the parameter d sets the width of the sharp maximum in the angular dependence $g(\theta)$; the parameter c defines the height of this peak; and the function $g(\theta)$ has a minimum at $h = \cos \theta$.

The Tersoff potential parameters determined for the case of sp^3 hybridization can be used to describe the interactions in materials with sp^2 hybridization [19].

The Si–Si interactions between atoms belonging to different silicene sheets were described by the Morse potential [20]

$$\Phi(r) = D_e [\exp\{-2\alpha(r - r_e)\} - 2 \exp\{-\alpha(r - r_e)\}], \quad (3)$$

Table 1. Morse potential parameters describing various interactions

Interaction	D_e , meV	α , nm ⁻¹	r_e , nm
*Si ⁽¹⁾ –Si ⁽²⁾	227.40	44.992	0.154
Si–C	925.20	20.820	0.253
Li–C	1258.51	17.074	0.206
Li–Si	309.30	36.739	0.116

The superscript indicates belonging to the first or second silicene sheet.

where D_e is the potential well depth, α is the rigidity parameter, and r_e is the equilibrium bond length. The interaction between the Li⁺ ion and Si and C atoms was also presented by the Morse potential. The parameters of this potential was determined from the corresponding data for describing Li–Li [20], Si–Si [21], and C–C [22] interactions. If Morse potential parameters for the representation of the interactions between atoms of type A and B , the parameters AB of interactions are found from the simple interpolation relations [21]

$$D_e^{AB} = (D_e^A D_e^B)^{1/2},$$

$$\alpha^{AB} = \frac{1}{2}(\alpha^A + \alpha^B), \quad (4)$$

$$r_e^{AB} = (r_e^A r_e^B)^{1/2}.$$

The Morse potential parameters used in this study are listed in Table 1.

Based on the scanning tunneling microscopy data, it was found that various regions of monolayers Si on Ag(111) surfaces after reconstruction have different structures [23, 24]. Among them, the largest area was occupied by the structure defined as (4×4) silicene/Ag, which corresponds to the silicene supercell (3×3) on the Ag (4×4) supercell. This structure consists of 18 Si atoms arranged in two sublattices. The unit cell of such a rhomb-shaped silicene structure contains 18 Si atoms. Six Si atoms of the unit cell are displaced to a distance of 0.064 nm perpendicular to the surface; other Si atoms are on the same (initial) plane. Si atoms protrude from the initial surface are displaced upward in the upper sheet of two-layer silicene, whereas such atoms in the lower sheet are displaced downward. We performed a number of calculations of the silicene channel to choose an optimum distance h_g between silicene sheets. The calculations were performed from the gap $h_g = 0.60$ nm to $h_g = 0.85$ nm with the step $\Delta h_g = 0.05$ nm. The electric field strength was 10^5 V/m. The ion began to completely pass through the channel at the gap $h_g = 0.70$ nm. This gap significantly exceeds the distance of 0.2481 nm between two-layer silicene sheets with AB packing obtained from calculations within the density functional theory [25]. In what follows, to study the ion

motion in the defect silicene channel, the gap variation range was decreased to $0.70 \leq h_g \leq 0.85$ nm.

Perfect silicene sheets containing 300 atoms each were rectangular-shaped, 4.7×4.0 nm (twelve atoms were arranged along each sheet edge). Nine mono- or polyvacancies were arranged approximately uniformly on the silicene sheet area, so that the number of Si atoms in each sheet was 291, 282, 273, and 246 for sheets with mono-, bi-, tri-, and hexavacancies, respectively. The dc electric field of 10^5 V/m accelerated Li^+ ions along the $0x$ axis oriented toward “zigzag” silicene sheets. Silicene sheets were arranged according to Bernal stacking of (ABAB...) using exactly the same method as in bulk graphite. Graphene sheets were arranged in parallel to silicene sheets outside the channel. Therewith, the distance between silicene and graphene sheets was the same as in [24], i.e., 0.286 nm. Frontal edges of silicene sheets and graphene ones were brought into coincidence. Each rectangular graphene sheet contained 820 atoms; along its each edge, 20 C atoms were arranged. The initial ion position corresponded to the height $h_g/2$. At $t = 0$, the ion was at the point with coordinates $x = 0.198$ nm, $y = 2.245$ nm; i.e., it was slightly pushed into the silicene channel approximately in the middle of the sheet width.

Standard codes of the LAMMPS program allow calculations so long as all system particles are in a given closed space. Calculations are ceased if at least one particle leaves this space. In order that this would not occur, the studied functional model of the silicene electrode was placed into a rectangular container. Furthermore, the distance from any Si or C atom belonging to the silicene–graphite system boundary to the nearest container wall was no less than 0.5 nm at the initial time. The distance from Si atoms of the upper silicene sheet to the upper container wall was 1.15 nm. Li^+ ions interacted with the wall only when it approached the wall to a distance of 0.25 nm. The Lithium ion could interact with the container wall according to the Lenard–Jones potential (12–6) with the parameters $\sigma = 0.1$ nm and $\epsilon = 1$ eV. These parameters are unrelated to any real material and are chosen empirically to obtain an adequate model reproducing the ion motion in the silicene channel. If the distance to the wall was less than 0.1 nm, the repulsive force affected the atom (ion), and its motion direction eventually changed to the opposite one. The equations of motion were numerically solved by the fourth-order Runge–Kutta method with time step $\Delta t = 1 \times 10^{-16}$ s. The duration of each calculation with the gap h_g was 1 million time steps. The silicene channel with gap $0.70 \leq h_g \leq 0.85$ nm was positioned on the graphite substrate.

To calculate the stresses appearing in silicene, sheets were divided into elementary areas. The stresses $\sigma_{n\alpha}(l)$ arising under the action of forces in the α direction (α takes the values x, y, z) are calculated on each

area with number l , having orientation n . In these calculations, the product of the projections of atomic velocities and projections of forces f_{ij}^α acting on the area l from the side of other atoms provided that the corresponding conditions are satisfied [26],

$$\sigma_{n\alpha}(l) = \left\langle \sum_i^k \frac{1}{\Omega} (mv_n^i v_\alpha^i) \right\rangle + \frac{1}{S_l} \left\langle \sum_i^k \sum_{\substack{j \neq i \\ (u_i \leq u, u_j \geq u)}} (f_{ij}^\alpha) \right\rangle. \quad (5)$$

Here k is the number of atoms on the area with number l , Ω is the atomic volume, m is the atomic mass, v_α^i is the α -projection of the velocity of the i th atom, S_l is the l th area. The conditions of summation over j in the last sum of expression (2) are reflected in both sum subscript and superscript; the force arising the interaction of atoms i and j passes through the l th area; u_i is the current coordinate of the i th atom, u in the sum superscript denotes the coordinate of the intersection of the straight line passing through the centers of atoms i and j with area l .

A structural analysis of small objects can be performed using the statistical geometry method based on constructing Voronoi polyhedra (VP) [27]. In the case of a multiatomic system, atoms of the same type can play the role of polyhedron centers, and atoms of the other type are used to determine polyhedron faces. For example, in the case of the “Li-silicene channel” system, it is convenient to use the lithium atom as a center and to choose the nearest neighbors among Si atoms. Such hybrid polyhedra can be almost always constructed, since Si atoms are on both sides of the Li atom, and silicene sheets do not represent an ideal plane. However, hybrid polyhedra are not Voronoi polyhedra in this case, since they do not completely occupy the entire space occupied by molecules, without voids and bridges. VP faces define cyclic structures formed of atoms of the same type as the central atom (VP center); whereas the faces of considered hybrid polyhedra with the center coinciding with the Li atom site define rings consisting of Si atoms. The Voronoi polyhedra can be constructed in a multicomponent system as well, if sizes of all atoms are identical. We will not consider the difference in Li and Si atom sizes when constructing polyhedra; i.e., we will consider VP.

The Voronoi polyhedra construction method can be used not only to study the short-range order structure of a “infinite” or finite objects, but also to trace the short-range order in the channel relief when moving the lithium ion in it. To this end, the constructed polyhedron center should be made coincident with the Li ion, and Si atoms of the channel in which the ion moves are chosen as geometrical neighbors for the ion. Polyhedra are constructed at regular time intervals until the ion leaves the channel. Finally, the ion motion in the channel under a dc electric field can be presented as distributions of Voronoi polyhedra elements. A comparison of such distributions obtained for various channels will provides some insight into the

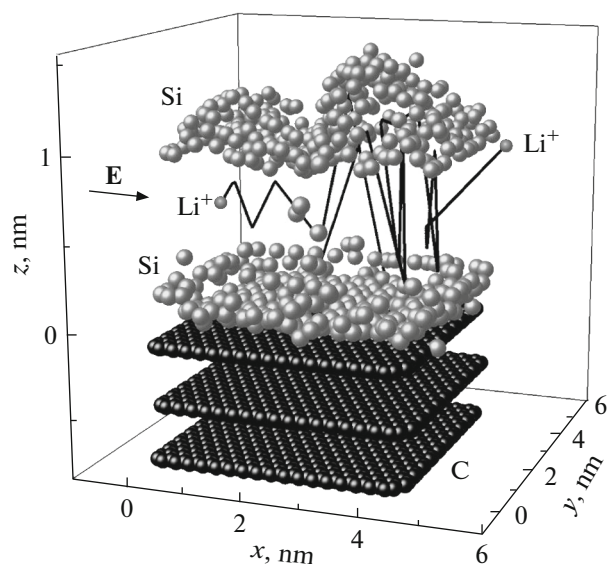


Fig. 1. Configuration of the system “coupled silicene sheets with divacancies on graphite” at the initial gap between sheets $h_g = 0.80$ nm is shown together with the lithium ion trajectory in the channel for 32.5 ps. A dc electric field acts along the $0x$ axis.

causes of the stopping effect caused by the channel. Therefore, we will refer to such a study as the statistical geometrical method for representing the stopping effect in the channel.

3. CALCULATION RESULTS

The general view of the system “coupled silicene sheets with divacancies on graphite” in 32.5 ps from the input into the channel with the initial gap $h_g = 0.80$ nm of the Li^+ ion is shown in Fig. 1. The Li^+ ion entering the channel on the left side (see Fig. 1) executes not only horizontal, but also vertical displacements, moving in an electric field whose strength vector is directed along the $0x$ axis. We can see that appreciable vertical displacements of Si atoms occur during the calculation in both upper and lower silicene sheets. Therefore, displacements increase from silicene with monovacancies to silicene with hexavacancies. A similar pattern is observed for systems with Ag(001) and Ag(111) substrates [15]. In the presence of both silver and graphite substrates, Si atoms are rearranged in the plane of the lower silicene sheet. On silver substrates, significant structural transformations are observed in the presence of defects in the upper silicene sheet.

Figure 2 shows the projections onto the xy plane of the upper and lower silicene sheets with trivacancies at $h_g = 0.80$ nm, obtained by the time of 100 ps. Silicene was placed on the graphite substrate. One can see that the substrate significantly affects the lower silicene sheet structure whose snapshot strongly changes to the calculation end. At the same time, the upper sheet

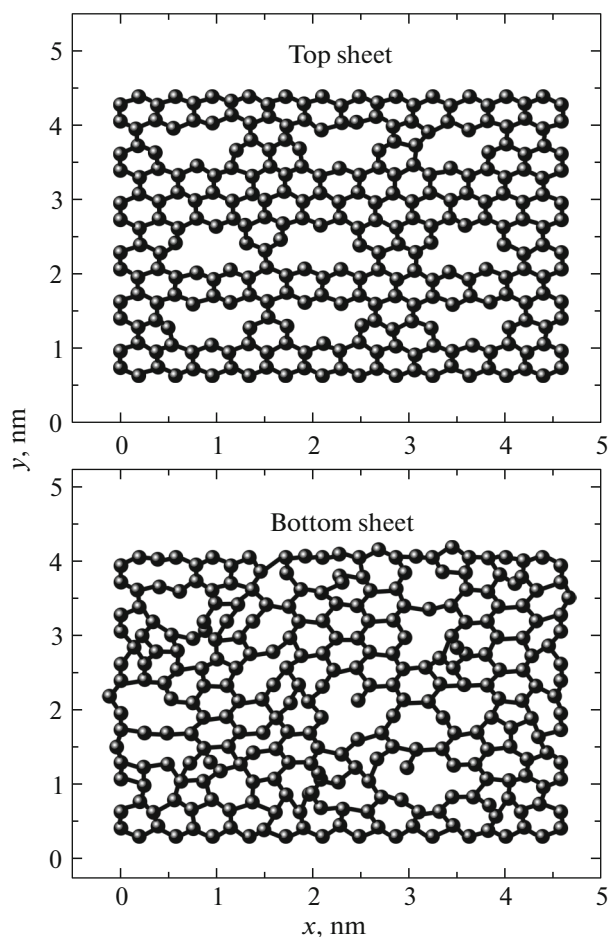


Fig. 2. Projections onto the xy plane of the upper and lower silicene sheets with trivacancies on the graphite substrate with interlayer gap of 0.75 nm at the time point of 100 ps.

retained not only all nine defects, but also, to a large extent, their size and shape. The number of pores in the lower silicene sheet lying on the substrate increased, but the size of most pores became smaller than the size of the initial trivacancy. Most pores formed in lower silicene have winding boundaries; however, there exist pores with smooth boundaries. It is worth noting atoms with two dangling bonds appeared in the strongly transformed structure of the lower sheet. Thus, the lattice mismatch of silicene and graphene (graphite surface) significantly affects the defect silicene structure after passing throughout the channel by the lithium ion.

Angular distributions of the geometrical neighbors encountered in the ion path in channels with perfect silicene walls and with silicene sheets containing bi- and hexavacancies are shown in Fig. 3. Angles with ions at their vertices and sides link it with the geometrical neighbors are considered. We can see that these characteristics significantly change not only with the defect density of channel walls, but also with varying its gap. As a rule, the intensity of peaks lying in the

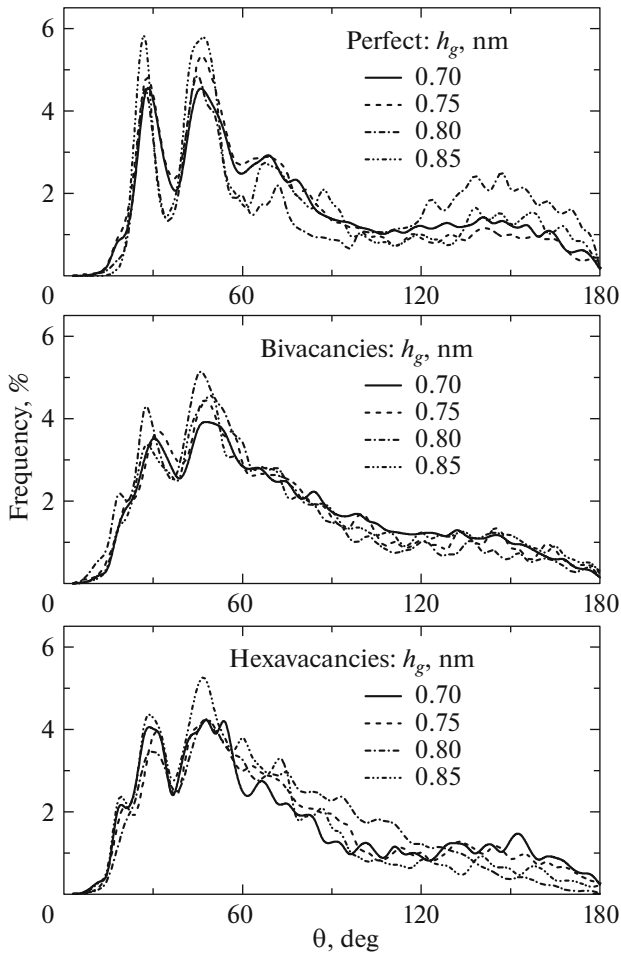


Fig. 3. Angular distributions of geometrical neighbors of the Lithium ion during its motion in various silicene channels.

vicinity of angles of 30° and 45° is enhanced with increasing gap. However, the growth of these peaks is retarded with increasing defect sizes. These peaks are formed due to the farthest geometrical neighbors. The number of such neighbors increases with channel expansion, and decreases with increasing defect size. The behavior of these peaks is mostly caused exactly by these factors. In the angular range $120^\circ \leq \theta \leq 180^\circ$, angular spectra show high stability as the channel gap increases, since the channel expansion weakly affects the number of the nearest geometrical neighbors of the ion.

Figure 4 shows the distributions of VP formed around the Li^+ ion moving in the channel over the number of faces. These distributions also characterize the number of Si atoms arriving at the nearest neighborhood of the Li^+ ion. In the case of the channel with walls of perfect silicene, the Li^+ ion most often appears surrounded by nine Si atoms, if the gap $h_g \leq 0.75$ nm.

However, as the gap increases, the definiteness in the determination of the highest numbers of Si atoms surrounding the ion decreases. For example, at $h_g = 0.80$ nm, the Li^+ ion environment of 13 and 15 Si atoms is most widespread; at $h_g = 0.85$ nm, the Li^+ environment of four Si atoms dominates.

The formation of vacancy defects in channel walls makes the Si ion environment even more unpredictable. Only in the channel formed by silicene sheets with monovacancies, with $h_g = 0.70$ nm, the ion environment of fifteen Si atoms is most probable. In other cases, as a rule, there is high uncertainty in the determination of this characteristic.

Exclusion of small geometrical elements in Voronoi polyhedra made it possible to turn to an analysis of more probable geometrical neighbors detected in the Li^+ ion environment. Truncated polyhedra without small faces have more compact n -distributions with maximum values $n < 25$ (Fig. 5). However, it is difficult to find a systematic feature in the dependences of the number of the most probable faces on the silicene channel gap h_g and on the defect density in silicene sheets in this case as well. We can see in Fig. 5 that peaks with intensities higher than 15% exist only in n -distributions for the channel with perfect walls and with walls containing monovacancies.

The distribution of rings formed by Si atoms around the Li^+ ion moving in the channel with walls of perfect and defect silicene at various gaps h_g (m -distribution) is shown in Fig. 6. For the gap $h_g = 0.70$ nm, the m -distribution peak shifts from $m = 10$ to $m = 5$ and 4 when going from the channel with perfect silicene walls to the channel with walls containing bivacancies and hexavacancies, respectively. In other cases shown in Fig. 6, the m -distribution maximum is in the range $3 \leq m \leq 6$. The effect of bi- and hexavacancies on the formation of the short-range order around the Li^+ ion moving in the channel appears most appreciable in the narrowest channels among the considered ones (at $h_g = 0.70$ nm).

The statistics of m -membered rings existing around the moving Li^+ ion becomes significantly clearer in the case of the transition from Voronoi polyhedra to truncated polyhedra. Figure 7 shows the distributions for truncated polyhedron faces (m_{tr} distributions) characterizing the Li^+ ion motion in silicene channels with various gaps, whose walls are formed by sheets of perfect and defect silicene. In this case four-membered rings dominate in the narrowest channels among the considered ones (with $h_g = 0.70$ nm) irrespective of whether its walls contain defects.

Four- and five-membered rings are most frequent in other cases shown in Fig. 7. Therefore, channel expansion more often gives rise to the m_{tr} -distribution peak at $m_{\text{tr}} = 5$.

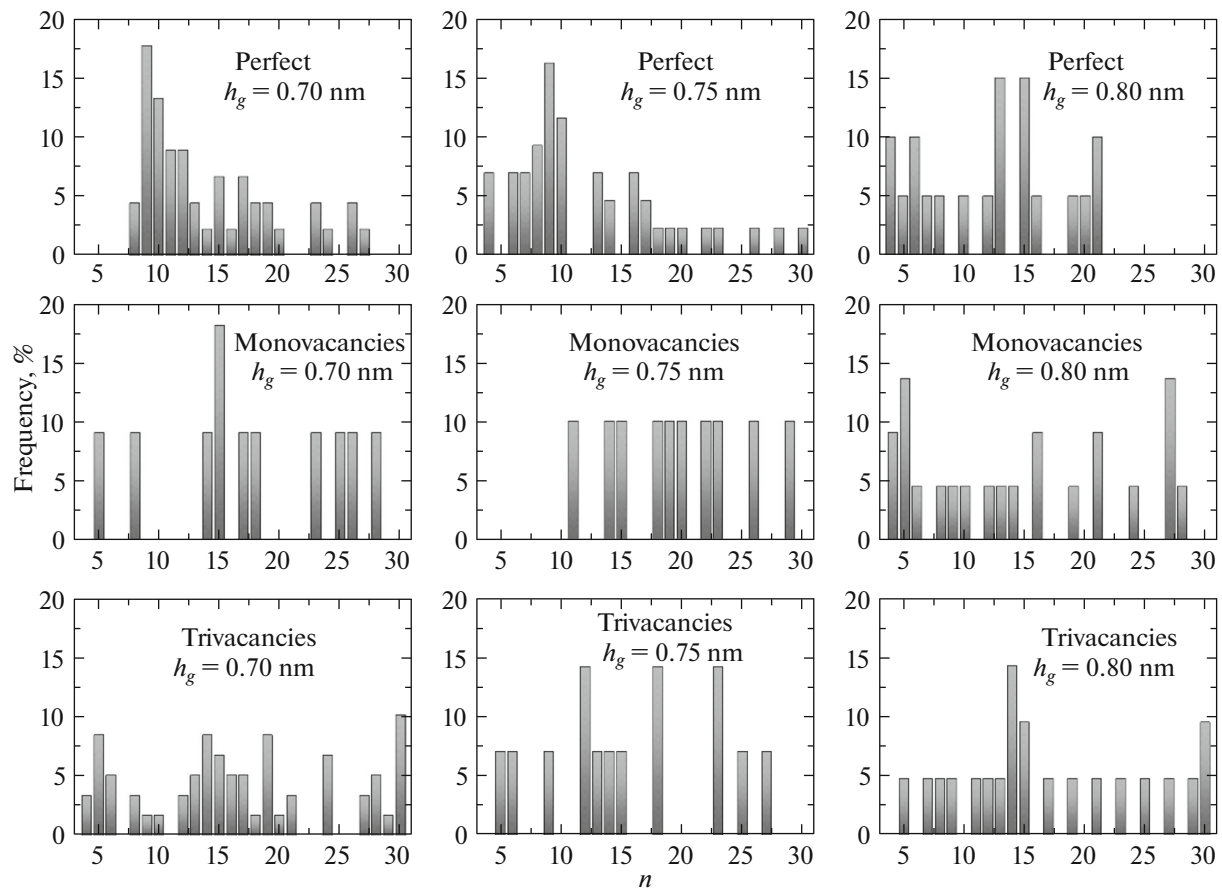


Fig. 4. Occurrence frequency of the number n of Si atoms included in the nearest geometrical neighbors of ion Li^+ during its motion in the perfect silicene channel and the channel with walls containing various vacancy defects. h_g is the silicene channel gap width.

The distributions of distances (r -distributions) to the nearest geometrical neighbors of the Li^+ ion at various gaps and channel types are shown in Fig. 8. The defect formation in channel walls results in a decrease in the standard deviation of the r -distribution. On average, the decrease in the standard deviation in the channel of defect silicene in relation to the channel of perfect silicene is 19%. A change in the channel gap causes an ambiguous change in the distance r_{mp} from the ion to the most probable geometrical neighbor. The channel gap-averaged value r_{mp} is 0.588, 0.542, and 0.546 nm for the perfect silicene channel and channels with mono- and hexavacancies, respectively.

The distribution of the most significant stresses $\sigma_{zz}(x)$ acting in the silicene sheet plane during the Li^+ ion motion in the channel is shown in Fig. 9. Elementary areas are extended along the $0y$ axis. The electric field of 10^5 V/m acts along the $0x$ axis.

Here an explicit dependence of the stress σ_{xx} fluctuation intensity on the channel gap and on the type of defects existing in silicene is not traced. Since the forces creating the stress σ_{zz} are as a rule downward

due to silicene attraction to the graphite substrate, the stresses σ_{zz} are almost always negative. The strongest local stresses appearing during the Li^+ ion motion in the channel is no more than 1.65 GPa or 0.693 N/m in magnitude. This value is 8.4 times lower than the silicene ultimate tensile strength obtained in [28]. Thus, when the Li^+ ion moves in the channel formed by perfect or defect silicene sheets, dangerous local stresses capable of silicene fracture do not appear.

4. DISCUSSION

The Li^+ ion motion in the planar silicene channel is much more complicated than in the similar graphene channel. For example, an electric field strength $E = 10^3$ V/m is sufficient for the Li^+ ion passage through the perfect graphene channel ~ 4 nm long without substrate at the intersheet gap $h_g = 0.60$ nm [29]. The lithium ion entirely passes through the perfect silicene channel in vacuum at $E = 10^5$ V/m, beginning from the gap between channel walls $h_g = 0.75$ nm [30]. The Li^+ ion motion in the silicene channel is

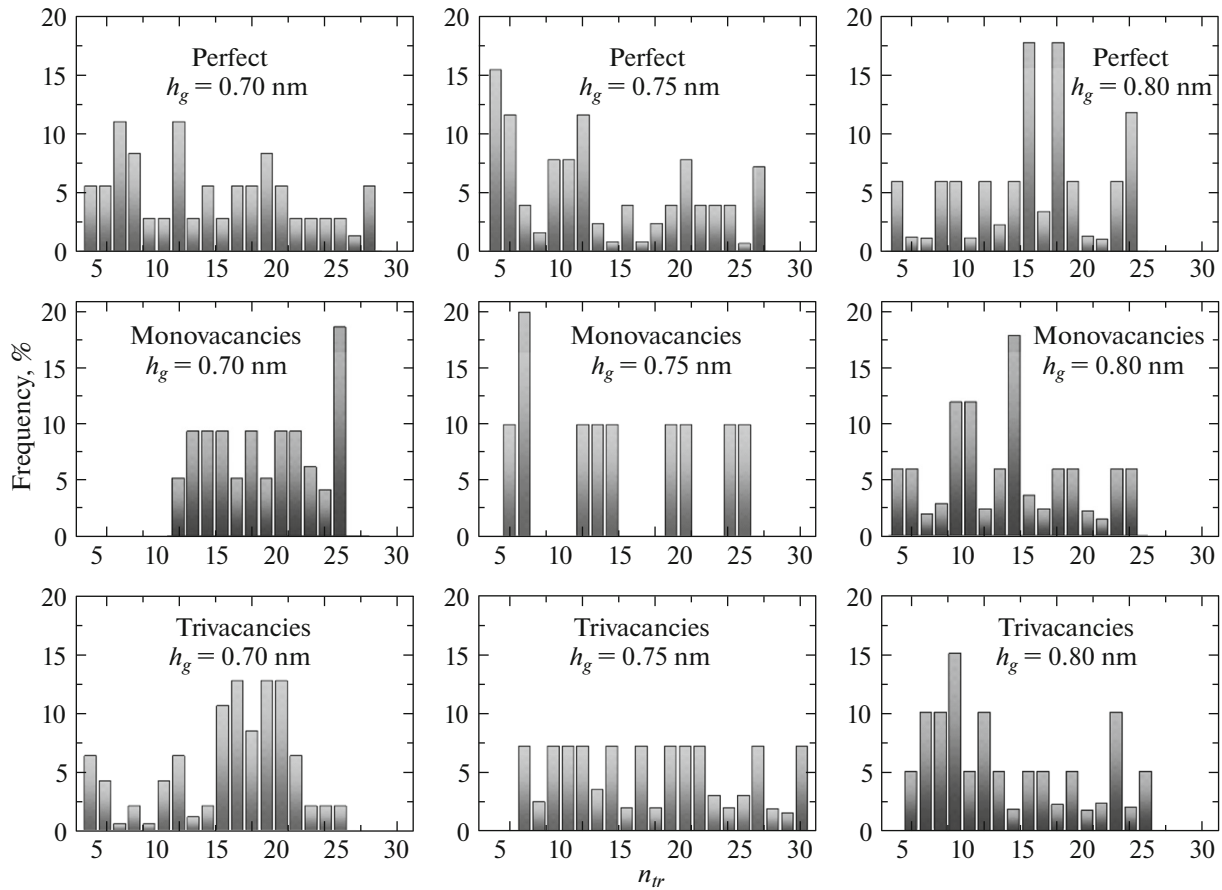


Fig. 5. Occurrence frequency of the number n of Si atoms included in more probable geometrical neighbors of the Li^+ ion during its motion in the perfect silicene channel and the channel with walls containing various vacancy defects. h_g is the silicene channel gap width.

even more complicated in the case of the presences of vacancy-type defects in channel walls. For example, at the gap $h_g = 0.80$ nm and field strength $E = 10^5$ V/m, the ion passes through the channel in a time shorter than 35 ps, if its walls contain mono- and bivalencies, but cannot leave the channel in the presence of tri- and hexavacancies in its walls even for 100 ps [31]. In the case where defect silicene was supported on both sides by single-layer perfect graphene, the lithium ion fully passed (for a time of <65 ps) through a narrower channel ($h_g = 0.75$ nm) with walls including mono- and bivalencies. However, the Li^+ ion could not overcome such a channel with walls containing tri- and hexavacancies for 100 ps [32]. Thus, the use of silicene instead of graphene as an anodic material requires expansion of the gap between adjacent sheets and a significant increase in the electric field strength.

In this study, we found that an even narrower silicene channel with gap $h_g = 0.70$ nm provides the lithium ion passage at an electric field strength of 10^5 V/m if the channel is supported by a graphite substrate. In this case, the channel passableness is retained not only

in the presence of mono- and bivalencies in its walls, but also in the presence of tri- and hexavacancies. The times of lithium ion passage through the silicene channel on the graphite substrate are listed in Table 2.

The longest time for assignment through the channel with a gap of 0.70 nm (74.5 ps) was observed when its walls contain bivalencies. The Li^+ ion remains in the silicene channel with gap $h_g = 0.75$ nm and walls containing bivalencies for 100 ps, but rather rapidly passes through this channel (more rapidly than for 36 ps) in the presence of tri- and hexavacancies in its walls. Trivacancies in the channel walls do not prevent Li^+ ion passage throughout it at all considered gaps (0.70–0.85 nm) for a time, not exceeding 64 ps. In the case of hexavacancies, the channel impassability for 100 ps arises only at gap $h_g = 0.80$ nm. The strong interaction with the substrate breaks the lower and upper sheets of both the perfect and defect silicene on Ag(001) and Ag(111) substrates and makes this material inapplicable for designing the lithium-ion battery anode [15]. Thus, the use of a graphite substrate to support the silicene channel creates better channel

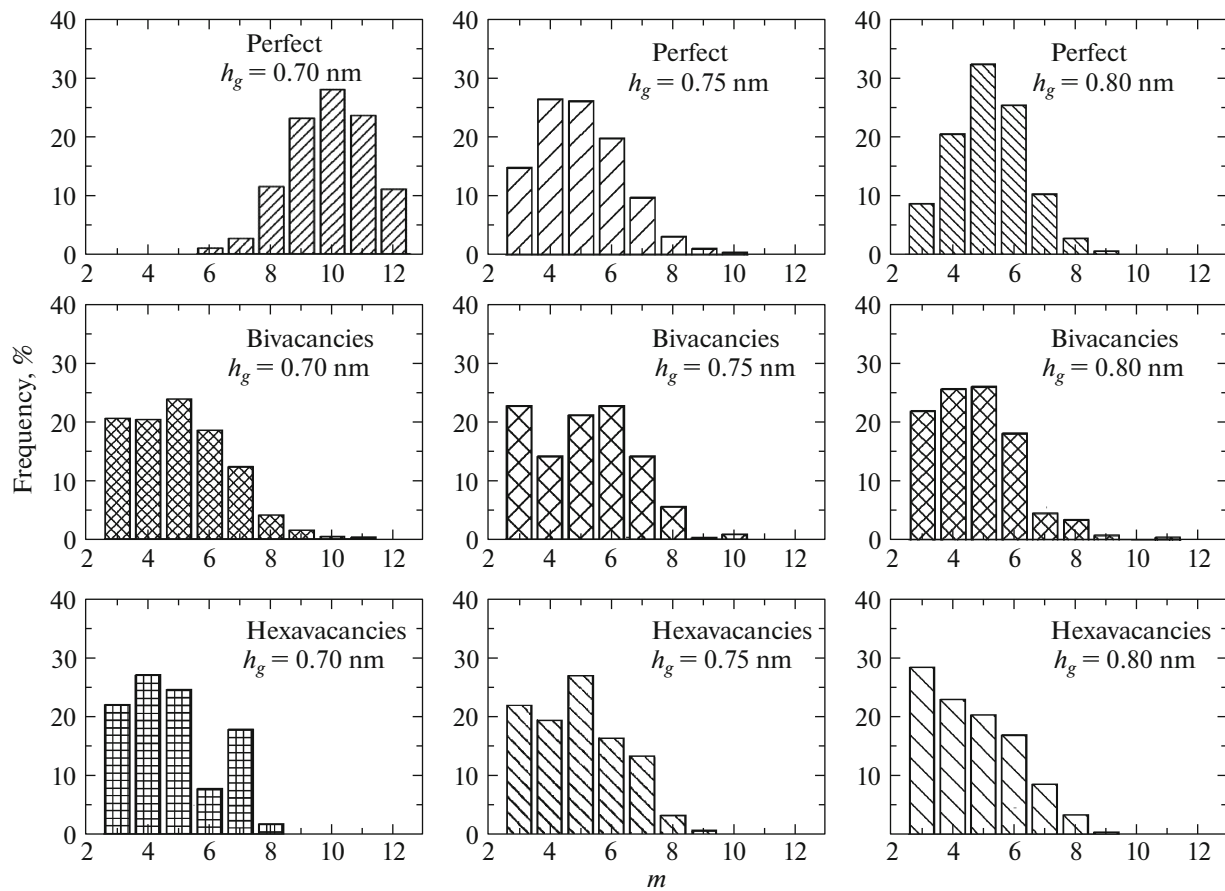


Fig. 6. Number of Si atoms forming rings around the Li^+ ion in channels with various gaps whose walls contain various defects.

passability for a lithium ion, than the use of a silver substrate or double-sided support of the silicene channel by graphene sheets.

In all cases at hand, the Li^+ ion motion in the silicene channel cannot be considered as particle motion in a disordered medium.

This is indicated by the appearance of two peaks with positions of $<50^\circ$ in the angular distribution of the nearest geometrical neighbors. For disordered systems, there exists only one peak in this region [33]. The calculated distributions of polyhedra over the number of faces are extended to a wide range of values

reaching $n = 30$ in some cases. Such behavior of the n -distribution is also uncharacteristic of disordered systems. Furthermore, many calculated n -distributions have a large number of equiprobably distributed face types. The latter feature is most likely a 2D-system specific which is retained when going to the consideration of statistical distributions for truncated polyhedra. The shape of the distribution of VP faces over the number of sides is controlled to a large extent by both the gap h_g and the type of channel wall defects. Both these characteristics also affect the shape of m -distributions constructed for truncated polyhedra.

Table 2. Time of lithium ion passage through the silicene channel on the graphite substrate, ps

Type of vacancies in silicene	Gap, nm			
	0.7	0.75	0.8	0.85
Perfect	45.4	42.2	20.4	73.6
Monovacancies	10.3	12.2	24.3	16.5
Bivacancies	74.5	Do not leave the channel	35.2	16.8
Trivacancies	64.0	13.8	21.2	25.9
Hexavacancies	16.7	18.2	Do not leave the channel	19.4

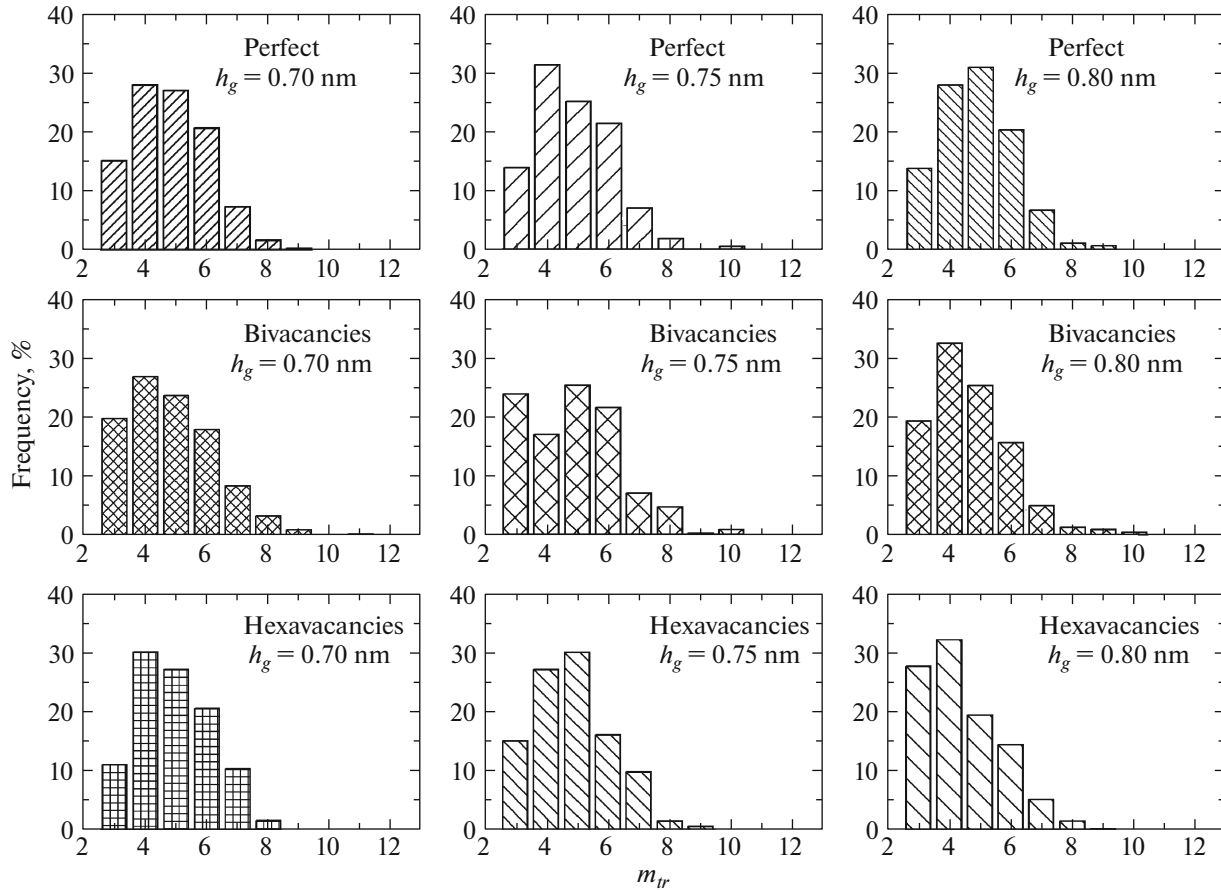


Fig. 7. Number of Si atoms forming averaged rings around the Li^+ ion in channels with various gaps whose walls contain various defects.

A similar statement is in general valid for distributions of distances from the ion to the nearest geometrical neighbors, i.e., Si atoms.

The silicene channel arrangement on graphite significantly reduces maximum local stresses arising in channel walls during the Li^+ ion motion. For example, the average value of $|\sigma_{zz}|_{\max}$ obtained for the silicene channel on graphite is lower than the similar characteristic found in the case of the channel on $\text{Ag}(001)$ and $\text{Ag}(111)$ substrates approximately by a factor of 2.4, and is 5.3 times lower than $|\sigma_{zz}|_{\max}$ determined when using a graphene support for the channel [15, 32]. The stress $|\sigma_{zz}|_{\max}$ reduction when using a non-metal substrate is associated with significantly weaker Si–C interactions in comparison with Si–Ag interactions. A sharp decrease in $|\sigma_{zz}|_{\max}$ in the case of the silicene channel on graphite can be explained by removal of its second wall from the substrate to a distance exceeding the distance between silicene and supporting graphene at least by a factor of 4.4. Furthermore, the initial distance between lower silicene layers and graphite $r_{\text{Si-C}} = 0.286$ nm was larger than the distance between silicene and graphene in the hybrid channel

(0.222 nm). Therefore, the covalent interaction was simulated between Si and C atoms in the silicene–graphene channel using the Tersoff potential; whereas, in this study, we consider the Van-der-Waals interaction between Si and C atoms. Due to the very weak effect of the graphite substrate on the upper silicene sheet, the structure of this sheet can be retained throughout the simulation even in the presence of large defects in the sheet, such as tri- and hexavacancies.

5. CONCLUSIONS

The method for studying the 2D material structure by moving a test particle along its planes, whose role is played by the lithium ion in the case at hand, was proposed. The method is based on the construction of Voronoi polyhedra whose centers coincide with the Li^+ ion site. Scanning of sheets of perfect silicene and silicene containing vacancy-type defects by moving the lithium ion in the channel, showed that the channel formed by sheets features a specific structure unlike to the structure of 3D ordered or disordered materials. The structure of layered 2D materials is

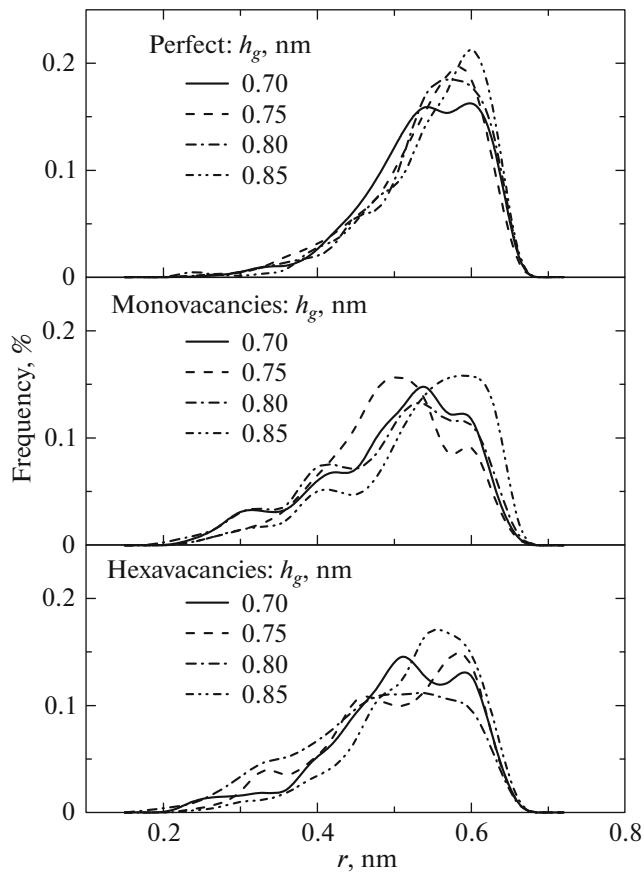


Fig. 8. Distribution of distances to the nearest geometrical neighbors of the Li^+ ion in the channel with perfect and defect silicene walls at various gaps.

characterized by the presence of two distinct peaks in the angular distribution of the nearest geometrical neighbors.

The positions of these peaks are subject to the condition $\theta_1, \theta_2 < 50^\circ$. The 2D silicon structure is described by a very wide set of the nearest geometrical neighbors determined for the moving center. Irrespective of the presence of defects of this or that type in silicene sheets, the number of geometrical neighbors for the lithium ion is in the range $4 \leq n \leq 30$. An appreciable existence of the equiprobable distribution of various geometrical neighbors is characteristic of n -spectra of 2D silicon. Depending on the gap width in the channel and the type of defects contained in its walls, the most probable Si-atom rings forming around the ion can contain from three to ten members. Elimination of small-scale fluctuations accompanying the ion motion reduces the range of the number of members in the abundant rings from four to five. Therewith, four-membered rings of geometrical neighbors are met more often than five-membered ones. The most probable distances from the ion to the nearest geometrical neighbors can be appreciably varied depending

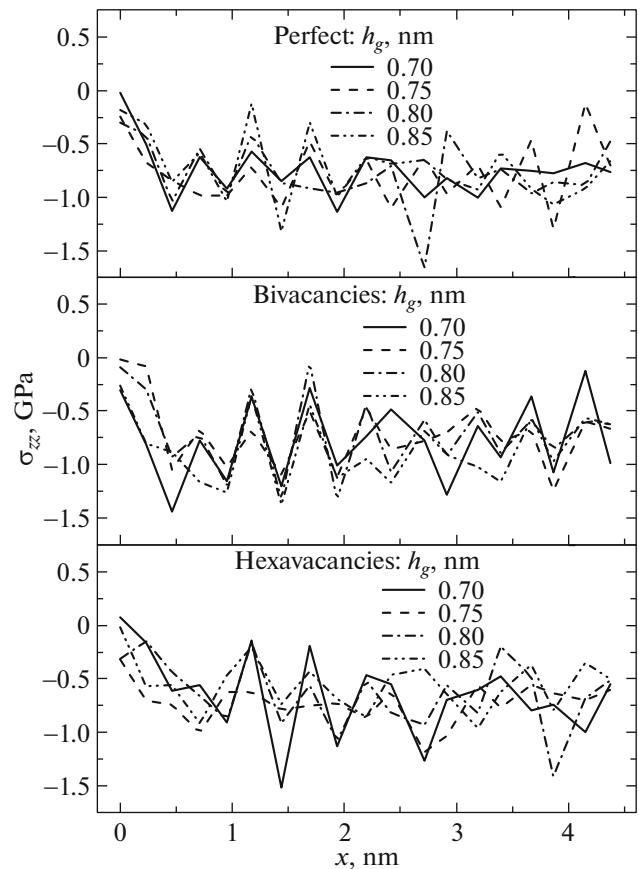


Fig. 9. Distribution of the stress $\sigma_{zz}(x)$ averaged over both sheets of perfect and defect silicenes, along the $0x$ axis (zigzag direction) coinciding with the electric field strength direction at various gaps.

on the gap in the channel and the type of defects contained in its walls.

The stresses σ_{zz} acting in the silicene sheet plane and caused by the forces perpendicular to this plane are most significant during the Li^+ ion motion along the silicene channel.

Local stress σ_{zz} changes are notably smaller than the ultimate strength of silicene during uniaxial tension.

Thus, coupled silicene sheets on the graphite substrate are applicable to the structure of the lithium-ion battery anode, including the case of silicene containing vacancy-type defects.

REFERENCES

1. Y. G. Guo, J. S. Hu, and L. J. Wan, *Adv. Mater.* **20**, 2878 (2008).
2. L. Ji, L. Zhan, M. Alcoutlabi, and X. Zhang, *Energy Environ. Sci.* **4**, 2682 (2011).
3. W. Xu, J. Wang, F. Ding, X. Chen, E. Nasybulin, Y. Zhang, and J. G. Zhang, *Energy Environ. Sci.* **7**, 513 (2014).

4. Y. Xie, Y. dall'Agnese, M. Naguib, Y. Gogotsi, M. W. Barsoum, H. L. Zhuang, and P. R. Kent, *ACS Nano* **8**, 9606 (2014).
5. W. Li, Y. Yang, G. Zhang, and Y. W. Zhang, *Nano Lett.* **15**, 1691 (2015).
6. H. R. Jiang, Z. Lu, M. C. Wu, F. Ciucci, and T. S. Zhao, *Nano Energy* **23**, 97 (2016).
7. D. Tsoutsou, E. Xenogiannopoulou, E. Golias, P. Tsipas, and A. Dimoulas, *Appl. Phys. Lett.* **103**, 231604 (2013).
8. L. Meng, Y. Wang, L. Zhang, S. Du, R. Wu, L. Li, Y. Zhang, G. Li, H. Zhou, W. A. Hofer, and H. J. Gao, *Nano Lett.* **13**, 685 (2013).
9. C. L. Lin, R. Arafune, K. Kawahara, M. Kanno, N. Tsukahara, E. Minamitani, Y. Kim, M. Kawai, and N. Takagi, *Phys. Rev. Lett.* **110**, 076801 (2013).
10. S. Cahangirov, M. Audiffred, P. Tang, A. Iacomino, W. Duan, G. Merino, and A. Rubio, *Phys. Rev. B* **88**, 035432 (2013).
11. S. Cahangirov, M. Topsakal, E. Akturk, H. Sahin, and S. Ciraci, *Phys. Rev. Lett.* **102**, 236804 (2009).
12. Y. Cai, C. P. Chuu, C. M. Wei, and M. Y. Chou, *Phys. Rev. B* **88**, 245408 (2013).
13. A. E. Galashev and K. A. Ivanichkina, *Russ. J. Phys. Chem. A* **91**, 2448 (2017).
14. M. Houssa and A. Molle, *J. Phys.: Condens. Matter* **27**, 253002 (2015).
15. A. E. Galashev, K. A. Ivanichkina, A. S. Vorob'ev, and O. R. Rakhmanova, *Phys. Solid State* **59**, 1242 (2017).
16. S. Plimpton, *J. Comp. Phys.* **117**, 1 (1995).
17. J. Tersoff, *Phys. Rev. B* **38**, 9902 (1988).
18. J. Tersoff, *Phys. Rev. B* **39**, 5566 (1989).
19. F. Benkabou, M. Certier, and H. Aourag, *Mol. Simul.* **29**, 201 (2003).
20. R. Yu, P. Zhai, G. Li, and L. Liu, *J. Electron. Mater.* **41**, 1465 (2012).
21. S. K. Das, D. Roy, and S. Sengupta, *J. Phys. F* **7**, 5 (1977).
22. T.-E. Fang and J.-H. Wu, *Comput. Mater. Sci.* **43**, 785 (2008).
23. B. Feng, Z. Ding, S. Meng, Y. Yao, X. He, P. Cheng, L. Chen, and K. Wu, *Nano Lett.* **12**, 3507 (2012).
24. D. Chiappe, C. Grazianetti, G. Tallarida, M. Fanciulli, and A. Molle, *Adv. Mater.* **24**, 5088 (2012).
25. M. Neek-Amal, A. Sadeghi, G. R. Berdiyrov, and F. M. Peeters, *Appl. Phys. Lett.* **103**, 261904 (2013).
26. A. Y. Galashev, *Comput. Mater. Sci.* **98**, 123 (2015).
27. V. P. Skripov and A. E. Galashev, *Russ. Chem. Rev.* **52**, 97 (1983).
28. R. Roman and S. W. Cranford, *Comput. Mater. Sci.* **82**, 50 (2014).
29. A. E. Galashev and Yu. P. Zaikov, *Russ. J. Phys. Chem. A* **89**, 2243 (2015).
30. A. E. Galashev, Yu. P. Zaikov, and R. G. Vladykin, *Russ. J. Electrochem.* **52**, 966 (2016).
31. A. Y. Galashev and K. A. Ivanichkina, *Phys. Lett. A* **381**, 3079 (2017).
32. A. E. Galashev, O. R. Rakhmanova, and Yu. P. Zaikov, *Phys. Solid State* **58**, 1850 (2016).
33. A. Y. Galashev, *J. Chem. Phys.* **139**, 124303 (2013).

Translated by A. Kazantsev